communications physics

Article

https://doi.org/10.1038/s42005-024-01795-3

Direct visualization of viscous dissipation and wetting ridge geometry on lubricant-infused surfaces

Check for updates

Abhinav Naga [1,2] ✉, Michael Rennick[1,2], Lukas Hauer [3], William S. Y. Wong [4], Azadeh Sharifi-Aghili[5], Doris Vollmer [5] ✉ & Halim Kusumaatmaja [1,2] ✉

Drops are exceptionally mobile on lubricant-infused surfaces, yet they exhibit fundamentally different dynamics than on traditional superhydrophobic surfaces due to the formation of a wetting ridge around the drop. Despite the importance of the wetting ridge in controlling drop motion, it is unclear how it dissipates energy and changes shape during motion. Here, we use lattice Boltzmann simulations and confocal microscopy to image how the wetting ridge evolves with speed, and construct heatmaps to visualize where energy is dissipated on flat and rough lubricated surfaces. As speed increases, the wetting ridge height decreases according to a power law, and an asymmetry develops between the front and rear sides. Most of the dissipation in the lubricant (>75%) occurs directly in front and behind the drop. The geometry of the underlying solid surface hardly affects the dissipation mechanism, implying that future designs should focus on optimizing the surface geometry to maximize lubricant retention.

Lubricants have been used for several millennia to reduce friction between solid surfaces[1,2]. In contrast, exploiting lubricants to minimize the friction between liquid drops and solid surfaces is a much more recent endeavor, driven by advances in surface fabrication techniques[3–5]. To understand how to control drop friction on lubricated surfaces, it is important to investigate the mechanisms of energy dissipation and how the properties of the lubricant and the geometry of the underlying solid surface influence these mechanisms.

Lubricated solid surfaces with low drop friction are typically called lubricant-infused surfaces (LIS) or slippery liquid-infused porous surfaces (SLIPS). Both SLIPS and LIS will be henceforth referred to as LIS in this paper. Typically, a LIS consists of micro/nanoscopic solid scaffold that is imbibed with lubricant. Drops barely stick on LIS because the lubricant fully spreads on the solid surface, masking underlying surface defects that would usually cause drops to stick if there was no lubricant. In this work, we consider both lubricated surfaces with and without microstructures. Comparing these two cases allows us to understand the role of the microstructures on the drop dynamics.

To initiate the motion of a water drop on LIS, the surface has to be inclined by merely ≈1–3°[6,7]. Due to their low friction, LIS have an impressive ability to repel a wide range of liquids, including low surface tension oils that cannot be repelled with traditional superhydrophobic surfaces inspired by the lotus leaf[8–10]. This non-stick property makes LIS potentially useful in technologies such as heat exchangers[11,12], medical devices[13,14], and self-cleaning surfaces[15–17].

Although drops begin to move at low tilt angles on LIS, they still experience significantly more friction during motion than on superhydrophobic surfaces (by around 1–2 orders of magnitude)[18–22]. On LIS, friction arises due to the complex interplay between capillary forces and viscous forces acting inside the drop and in the lubricant meniscus (called wetting ridge) surrounding the drop[23–28]. Previous works have suggested that most energy is dissipated in the wetting ridge and possibly in the lubricant film underneath the drop, rather than in the drop itself when the lubricant is more viscous than the drop[23–25,29,30]. Yet, this has not been shown directly.

The first aim of this paper is to construct dissipation heatmaps to visualize where energy is dissipated in the drop and lubricant. These heatmaps allow us to identify which regions within the wetting ridge must be considered when modeling the friction force.

Another key challenge in the design of LIS is to minimize the amount of lubricant that is carried away by the wetting ridge when drops slide off the surface[31,32]. Depletion of lubricant causes LIS to lose their low-friction functionality, making them unsuitable for long-term applications and

[1]Department of Physics, Durham University, Durham, UK. [2]Institute for Multiscale Thermofluids, School of Engineering, The University of Edinburgh, Edinburgh, UK. [3]Institute for Biology, Humboldt-Universität zu Berlin, Berlin, Germany. [4]Department of Applied Physics, School of Science, Aalto University, Espoo, Finland. [5]Physics at Interfaces, Max Planck Institute for Polymer Research, Mainz, Germany. ✉e-mail: abhinav.naga@ed.ac.uk; vollmerd@mpip-mainz.mpg.de; halim.kusumaatmaja@ed.ac.uk

products where contamination of the flowing liquid by the lubricant is undesirable, such as in food processing[26,33,34]. It is, therefore, important to understand how much lubricant is transported in the wetting ridge when drops move on lubricated surfaces.

The second aim of this paper is to directly image the shape and size of the wetting ridge at a wide range of drop speeds and lubricant viscosities. This allows us to understand how much lubricant is transported in the wetting ridge during motion.

To achieve these aims, we use a state-of-the-art lattice Boltzmann numerical method and a bespoke experimental setup based on laser scanning confocal microscopy. We focus on the common case where the lubricant is more viscous than the drop and consider cases where the underlying solid structure is either a flat surface or consists of a regular array of pillars. By systematically analyzing the dissipation heatmaps, we arrive at the following key findings. Firstly, the same friction laws are obtained for both flat and pillar solid geometries because their dissipation heatmaps share many similarities. Secondly, ≈75% of the dissipation in the lubricant occurs directly in front and behind the drop, with the rest being along the lateral sides of the drop. Thus, effective friction models can be obtained by considering only the front and rear sides of the wetting ridge. Finally, the size of the wetting ridge decreases with increasing speed and asymmetry develops between the two sides during motion. This implies that faster drops deplete less lubricant than slower drops.

Results and discussion

Friction force

We use a state-of-the-art lattice Boltzmann method to simulate the dynamics of drops on lubricated surfaces. With this method, we can simulate up to three fluids (drop, lubricant, and air) with tunable viscosities and surface tensions, and complex solid geometries (e.g., pillars) with tunable wetting properties (refer to Methods for details). We move the drop by applying a force parallel to the lubricated surface. To explore whether it is important to consider 3D simulations compared to 2D or quasi-3D simplifications, we simulate all cases. On the lubricated surface with pillars, 2D is equivalent to a cylindrical drop moving perpendicular to evenly spaced infinitely long grooves, whereas quasi-3D corresponds to a cylindrical drop moving across a rectangular pillar array. 3D corresponds to a hemispherical drop moving on a rectangular pillar array. On the flat lubricated surface, 2D and quasi-3D are equivalent. As will be discussed in more detail later, it turns out that the dissipation mechanism is unaffected by the dimensionality. However, full 3D simulations are required to capture the geometry of the wetting ridge accurately.

We apply periodic boundary conditions on the left and right sides of the simulation domain, however, we stop the simulations just before the drop crosses the periodic boundary. This is because the drop typically leaves a Landau-Levich lubricant film behind as it moves on the surface[7]. Thus, when the drop moves along the same trajectory for the second and subsequent times after crossing the periodic boundary, it experiences a different (larger) lubricant thickness. Due to this memory effect, we have to resort to using very large and computationally expensive simulations, particularly when simulating the drop shape in 3D (domain size ≈ 34× the drop volume, 9×10^6 lattice points).

The dimensionless parameter that characterizes the applied force and the drop velocity are the Bond number and the capillary number, respectively. The Bond number reflects whether the applied force influences the shape of the drop. It given by $\mathrm{Bo} = fR^2/\gamma$, where f is the force per unit volume applied to the drop, R is the initial drop radius, and γ is the surface tension of the drop/air interface. The capillary number compares the relative importance of viscous to capillary forces. It is given by $\mathrm{Ca} = \eta v/\gamma_{\mathrm{DL}}$, where η is the lubricant viscosity, γ_{DL} is the interfacial tension of drop/lubricant interface, and v is the drop velocity. In the simulations, $0.12 < \mathrm{Bo} < 1.15$ and $0.01 < \mathrm{Ca} < 1$. Unless otherwise stated, the lubricant is 10 times more viscous than the drop, the contact angle between the lubricant and the solid is 0° (fully wetting) both in air and under the drop, and the solid fraction of the pillars is 0.25 in the 3D simulations. The surface tensions of the drop and lubricant are chosen such that the macroscopic Neumann angle at the tip of the wetting ridge is similar to that in typical experimental systems consisting of water drops and silicone oil lubricant (≈10°).

To gain insight into the role of solid geometry, we start by comparing the macroscopic dynamics of drops on flat lubricated surfaces and LIS with pillars. In both cases, the initial thickness of the lubricant layer is equal to the pillar height on the surface that has pillars. Similar trends are obtained between the drop velocity and the applied force, regardless of the solid geometry, the dimensionality of the simulations, and whether or not the lubricant fully spreads on the surface of the drop to form a cloak [Fig. 1a]. In all cases, the relationship between the force and the capillary number can be described by the scaling law proposed by Keiser et al.[23] and Daniel et al.[25],

$$F \sim k\gamma w \mathrm{Ca}^{2/3}. \quad (1)$$

Here, F is the applied force, k is a numerical prefactor that depends on the geometry of the solid and the dimensionality of the system, w is the width of drop's base, and Ca is the capillary number corresponding to the steady-state drop velocity. Although the prefactor k depends on the precise details of the system, the exponent of the scaling relation is universal regardless of the dimensionality of the system and whether the solid substrate is flat or has a regular array of pillars.

Experimental measurements of the drop friction force reveal that at high capillary numbers ($\mathrm{Ca} > 10^{-2}$), the exponent of the scaling law between the friction force and the capillary number may decrease from 2/3 to 1/3[24,35]. This transition is not obtained in our simulations (see Supplementary Fig. 1, where we directly compare the friction force in our simulations to experiments). We expect this difference to be due to the discrepancy in the ratio between the wetting ridge height and the equilibrium film thickness above the solid structures. In the simulations, the film thickness is larger than in typical experiments[6,23,25] due to the nature of the diffuse interface, causing the ratio to be of the order of 10, whereas in the experiments it is of the order of 100 to 1000. Thus, the results presented throughout this paper correspond to the limit when the scaling law exponent is 2/3.

The non-linear relationship between force and velocity differs from the linear relationship observed on smooth, rigid and inert non-lubricated flat surfaces[36]. On non-lubricated surfaces that are flat, inert, and smooth, friction arises primarily due to capillary forces and viscous dissipation in the drop, as long as effects such as electrostatic retardation[37] and surface adaptation[38] are negligible. In contrast, on viscous lubricated surfaces, the majority of energy is dissipated in the lubricant [Fig. 1b]. At small Ca (≈0.05), over 80% of the energy dissipated is dissipated in the lubricant. Although this number reduces to ≈ 70% when Ca increases by a factor of 7, the dissipation in the lubricant always remains dominant. In all cases, the dissipation in the drop is only between ≈ 15% and 30% of the total dissipation in the drop and lubricant. This provides a rigorous basis for the hypothesis proposed by Keiser et al.[23] and Daniel et al.[25] that the majority of dissipation occurs in the viscous lubricant.

Velocity profiles

The universal scaling law exponent in Eq. (1) raises the question of whether the dissipation mechanism is the same regardless of the solid geometry. To investigate the underlying mechanisms in detail, we analyze the velocity profiles and viscous dissipation locally throughout the domain. Viscous dissipation arises when there are gradients in the local fluid velocity. As drops move on lubricated surfaces, liquid gets continuously reorganized in the drop and wetting ridge, causing energy to be dissipated. Previous numerical studies were unable to resolve viscous dissipation accurately due to the high level of numerical noise in the velocities close to the liquid/liquid interfaces. Resolving the velocity profiles close to the interfaces is particularly important when studying drop dynamics on lubricated surfaces because a significant proportion of the total dissipation is localized close to the lubricant/drop, lubricant/solid, and lubricant/air interfaces. Our lattice Boltzmann method enables us to resolve velocities as small as ≈ 1/1000 times the lowest drop velocity investigated (i.e., noise in the velocity

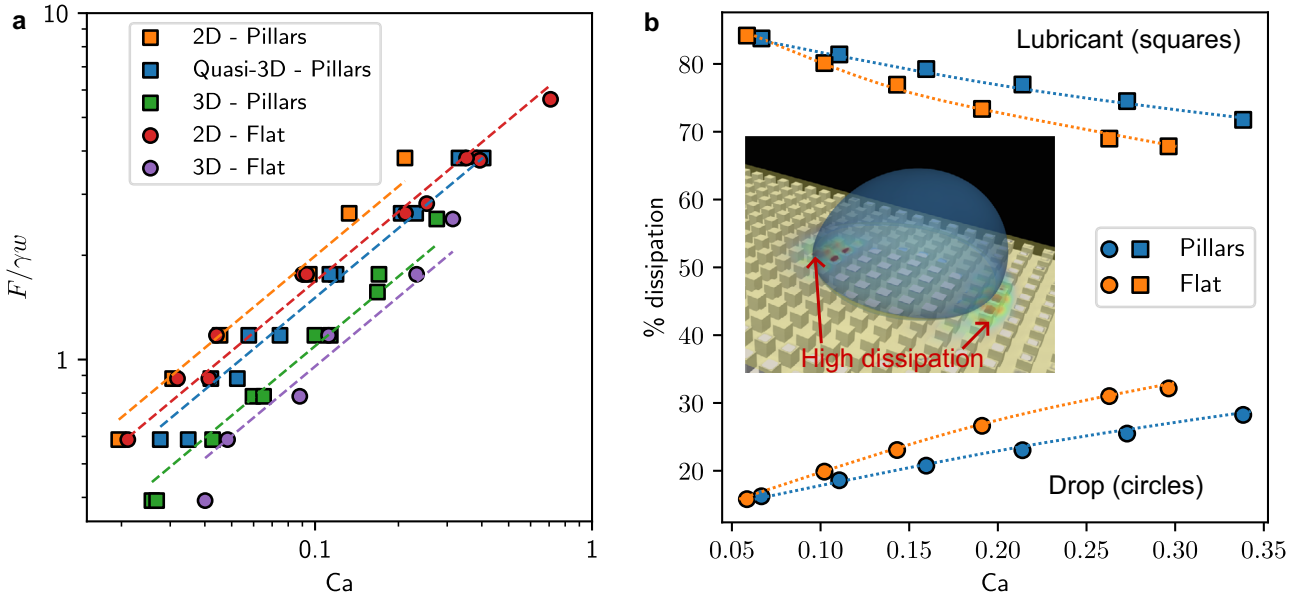

Fig. 1 | Macroscopic friction and dissipation. a Normalized friction force against capillary number on lubricated surfaces with flat (circles) and pillar (squares) geometries. Both 2D and 3D data are included. The 2D data includes different drop radii (R = 10× and 20× the pillar width) and also includes drops that are cloaked by lubricant. Quasi-3D corresponds to a cylindrical drop (long axis perpendicular to motion) spanning one pillar and one interstice along the long axis. **b** Energy dissipated in the drop and lubricant in 3D shows that most of the dissipation occurs in the lubricant. The percentages are relative to the total dissipation in the drop and lubricant. The inset shows a heatmap of viscous dissipation when a 3D drop moves on lubricated pillars. Red denotes high dissipation. Dissipation is highest at the front and rear sides of the drop, as shown by the red shadings marked by the red arrows. In the inset, Ca = 0.17, Bo = 0.6, the pillar width and edge-to-edge spacing are both 5 lattice units, and the drop radius is around 10 times the pillar width.

is insignificant; $\cong 10^{-6}$ in lattice units). This allows us to resolve the velocity profiles and calculate the viscous dissipation in all the fluid phases with very high accuracy.

When viewed in the center-of-mass frame of the drop, the flow in the drop follows a rolling motion (Fig. 2a). In the wetting ridge, lubricant flows horizontally around the sides of the drop and qualitatively resembles the flow around an obstacle (Fig. 2b). In the vertical direction, lubricant close to the drop/lubricant interface in the wetting ridge follows the rolling flow in the drop. At the front side, lubricant is dragged downwards whereas, at the rear side, it is dragged upwards along the drop/lubricant interface (Fig. 2c, d). In the absence of pillars, the velocity profiles are qualitatively similar, except that the lubricant right above the solid substrate flows parallel to the flat solid instead of being disturbed by the pillars (Supplementary Fig. 2).

The power dissipated per unit volume is related to velocity gradients according to,

$$P_{diss} = \frac{1}{2\eta}\left(\sigma_{xx}^2 + \sigma_{yy}^2 + \sigma_{zz}^2 + 2\sigma_{xy}^2 + 2\sigma_{yz}^2 + 2\sigma_{xz}^2\right). \quad (2)$$

Here, $\sigma_{\alpha\beta}$ is the viscous stress tensor, which is related to the velocity gradients according to[39],

$$\sigma_{\alpha\beta} = \eta\left(\frac{\partial v_\alpha}{\partial x_\beta} + \frac{\partial v_\beta}{\partial x_\alpha}\right), \quad (3)$$

where, η is the dynamic viscosity of the fluid and v_α is the velocity along the α direction ($\alpha = x, y, z$). The above expression tells us that two factors lead to high dissipation: large velocity gradients and high viscosities. Eq. (2) allows us to compute the dissipation locally at every point in the drop and lubricant to identify which regions dissipate the most energy. The uncertainty in the viscous dissipation in our simulations is over 5 orders of magnitude smaller ($\mathcal{O}(10^{-16})$ in lattice units per unit volume) than the actual dissipation arising in the wetting ridge during motion. This small uncertainty allows us to quantify the dissipation with high precision, which is essential to understand friction on lubricated surfaces.

Distribution of dissipation

Although the drop is significantly larger in volume than the wetting ridge, it dissipates less energy because the intensity of dissipation (dissipation per volume) is much smaller in the drop. While there exist some velocity gradients in the drop due to the rolling flow, these do not lead to significant dissipation because of the low drop viscosity compared to the lubricant (Eq. (2)). In contrast, the large velocity gradients in the wetting ridge combined with the high lubricant viscosity leads to a high dissipation.

On lubricated surfaces with pillars, dissipation is strongest just above the pillars close to the drop/lubricant interface (Fig. 3a, Supplementary Movie 1). In the wetting ridge, there are velocity gradients both horizontally due to the flow of lubricant around the drop, and vertically due to the flow of lubricant above the pillars and along the direction of the rolling flow in the drop. To identify which flow velocity gradients contribute the most to the dissipation, we analyze the 6 independent components of the viscous stress tensor separately and find that the σ_{xz} component dominates, where x is the direction of motion and z is perpendicular to the surface (Supplementary Fig. 3). Thus, dissipation is predominantly caused by gradients in the x component of velocity along the vertical direction.

The dissipation heatmaps for lubricated surfaces without pillars share many common features with those for the pillars (Fig. 3b, Supplementary Movie 2). In both cases, dissipation is predominantly localized directly in front and behind the drop. However, in the absence of pillars, the dissipation is most intense right behind the drop/lubricant interface at the rear of the drop, rather than being most intense on top of the pillars. The dissipation heatmaps remain qualitatively similar to the ones shown in Fig. 3 even when the lubricant fully spreads on the drop to form a cloak layer (Supplementary Fig. 4).

The dissipation heatmaps corresponding to 2D simulations also look similar to those for the 3D simulations for both surface geometries (Supplementary Figs. 5–8, Supplementary Movies 3, 4). However, we note that

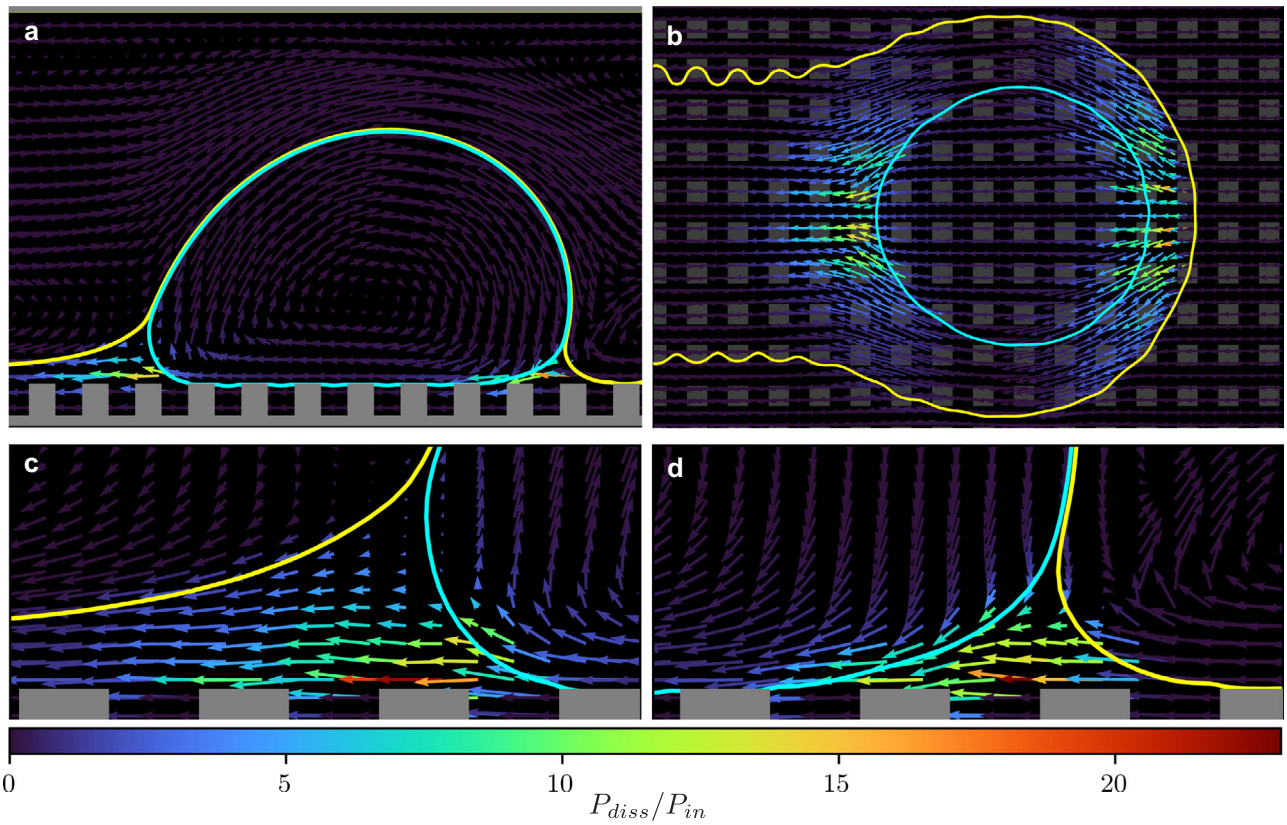

Fig. 2 | Velocity profiles for a three-dimensional drop moving to the right on lubricated pillars, as viewed in the center-of-mass frame of the drop. **a**–**d** Throughout this figure, Ca = 0.17, Bo = 0.6, and the lubricant (highlighted by the yellow contours) is 10 times more viscous than drop (cyan contours). The width of the pillars (in gray) is 5 lattice units. The length of the arrows is proportional to the magnitude of the velocity and the color of the arrows represents the ratio of the power dissipated at the position of the arrow to the power input per unit volume ($P_{in} = fv$) to drive the motion of the drop, as shown by the color bar at the bottom of the figure. **a** Velocity profile in a vertical slice through the center-of-mass of the drop indicates a rolling motion inside the drop. **b** Velocity profile in a horizontal slice just above (2 lattice units) the top of the pillars shows the flow of lubricant in the wetting ridge around the drop. **c**, **d** Zoomed-in perspective of the velocity profiles in (**a**), focusing on the rear and front wetting ridge, respectively.

two key differences exist between 2D and 3D. Firstly, the shape and sizes of the wetting ridge are different in the 2 cases because there is no pathway for lubricant to flow around the drop in 2D (Supplementary Fig. 9). Secondly, since there is no pathway for lubricant to flow around the drop in 2D, lubricant accumulates in the front wetting ridge, which may cause the front wetting ridge to become significantly larger than the rear side in 2D. In contrast, in 3D, the front wetting ridge is never larger than the rear. Furthermore, due to the buildup of lubricant in the front wetting ridge in 2D, more lubricant is forced to go underneath the drop, causing the thickness of the lubricant film underneath the drop to be larger in 2D than 3D for the same Ca. Therefore, full 3D simulations are required to quantitatively understand the shape of the wetting ridge.

The similarities between the dissipation heatmaps on lubricated surfaces with pillars and without pillars demonstrate why the scaling law between the drop velocity and the friction force is universal regardless of the solid geometry (as shown in Fig. 1a). The similarity in the heatmaps also supports previous experiments that have reported the same scaling law exponent for multiple solid geometries[23–25]. Contrary to common expectations, this demonstrates that the presence of lubricant is more crucial than the solid geometry in determining the friction laws on LIS.

The simulations of the flat lubricated surfaces can also be interpreted as corresponding to the limit where the lubricant thickness is significantly greater than the height of the solid structures such that the solid structures appear insignificant on the scale of the lubricant thickness. For example, this limit corresponds to the case when nanostructured surfaces are coated with an excess of lubricant whose thickness exceeds the height of the solid structures by at least 1-2 orders of magnitude, as originally fabricated by Wong et al.[4]. One key difference between having tall compared to short (or flat) solid structures is that it is easier to form a Landau-Levich lubricant film underneath the drop on surfaces with short structures. Yet, our results show that despite the presence of a noticeable Landau-Levich lubricant film underneath the drop on the flat surfaces, the locations that have the highest concentration of dissipated energy remain similar to what is observed in the absence of a prominent Landau-Levich film on the surfaces with pillars. Thus, the primary benefit of the solid structures is to help suppress lubricant depletion instead of changing the mechanism of dissipation.

To quantify the dissipation in different regions of the lubricant, we divide the wetting ridge and the lubricant film under the drop into 5 different zones (as defined in Fig. 3c). We define the dissipation zones loosely based on the regions considered by Keiser et al. when they described the friction mechanisms of drops on lubricated surfaces[23]. Here, we define the zones based on the position of the topmost point of the wetting ridge, (x_{top}, h_{top}). Zones 1 and 2 correspond to the leading (from x_{top} to $x_{top} + 2h_{top}$) and trailing (from $x_{top} - 2h_{top}$ to x_{top}) ends of the front wetting ridge, respectively. Zone 3 corresponds to the lubricant film underneath the drop only and excludes the lateral sides of the wetting ridge. Zone 4 and 5 correspond to the leading and trailing ends of the rear wetting ridge, respectively. Zones 4 and 5 are defined in a similar way to zones 1 and 2 except that the coordinates of the top of the rear, rather than the front, wetting ridge are used for x_{top} and h_{top}. To ensure that the 5 zones contain the majority (over 75%) of the total lubricant dissipation, we choose the width of the zones to be half the initial drop diameter, as shown in the

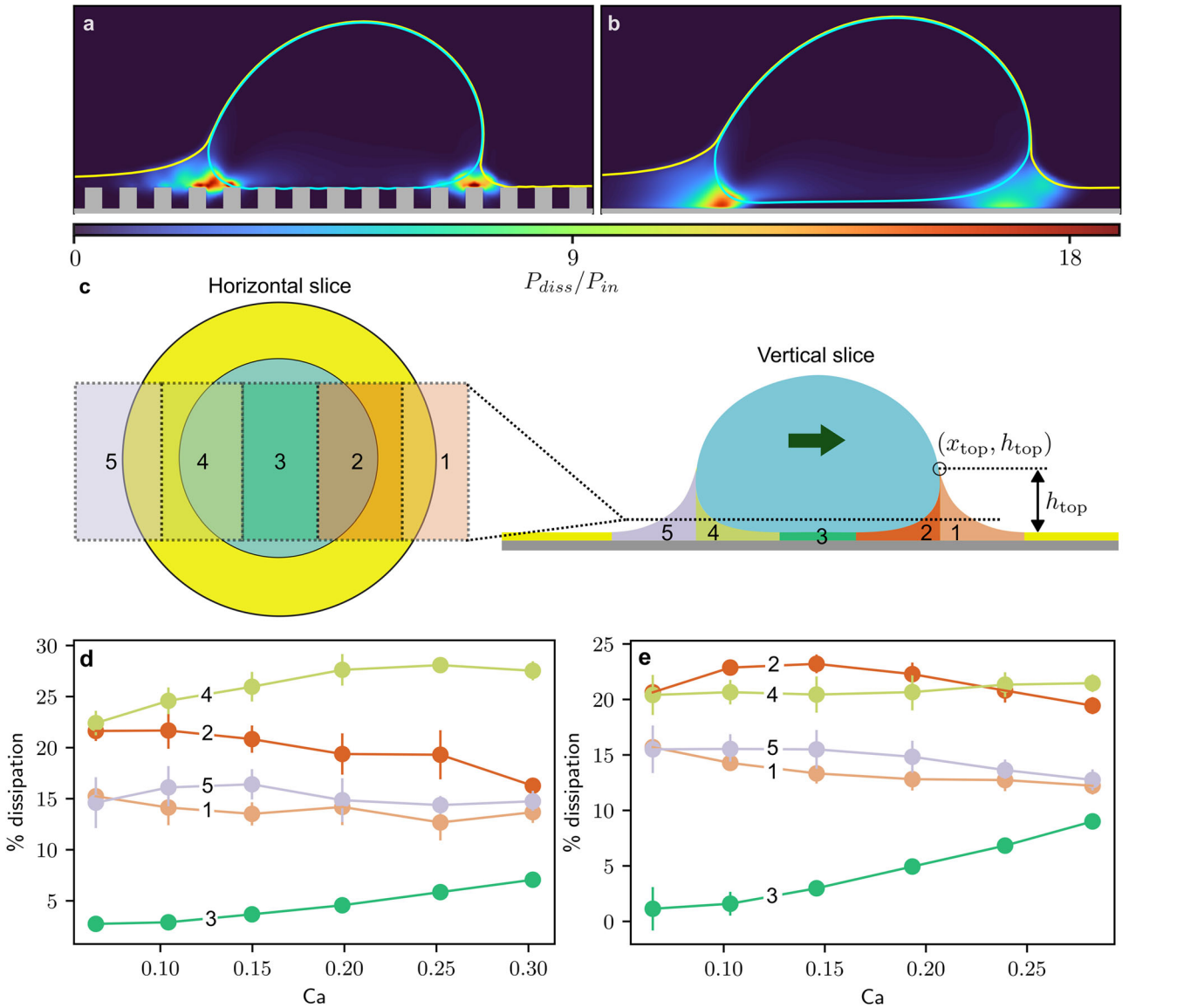

Fig. 3 | Distribution of viscous dissipation in the wetting ridge on lubricated surfaces with and without pillars. a–**e** Throughout this figure, the lubricant is 10 times more viscous than the drop and all simulations are in 3D. **a**, **b** Dissipation heatmaps on a lubricated surface with pillars (Ca ≈ 0.17) and without pillars (Ca ≈ 0.19), respectively. The heatmaps correspond to vertical slices taken across the center of mass of the drop. In both (**a**) and (**b**), the same force is applied to the drop (Bo = 0.6) and the initial lubricant thickness is the same (equal to the pillar height in **a**). In the colorbar, P_{diss} is normalized by the power per unit volume supplied to move the drop, $P_{in} = fv$. **c** Schematic showing how the 5 different dissipation zones are defined. **d**, **e** Percentage dissipation in the different zones of the wetting ridge (as defined in **c**) relative to the total dissipation in the lubricant on surfaces with and without pillars, respectively. On average, across the different Ca, zones 2 and 4 dissipate the most energy, followed by zones 1 and 5. Dissipation in zone 3 is typically < 10%. In (**d**) and (**e**), the error bars correspond to the standard deviation of the dissipation measured over several frames (typically 9) as the drop moves on the surface.

horizontal slice schematic in Fig. 3c. Note that, in general, the different zones do not have equal volumes.

For both flat and pillar surfaces, the majority of dissipation is localized in the wetting ridge (zones 1 + 2 + 4 + 5), with only 10% of the total dissipation occurring in the lubricant film underneath the drop (zone 3) (Fig. 3d, e). Dissipation in zone 3 is small because there are barely any velocity gradients in the lubricant film underneath the drop. The increase in the dissipation in zone 3 with capillary number is because the height of the wetting ridge decreases with speed, causing the volume of zone 3 to increase relative to the other zones.

Previous works have argued that the formation Landau-Levich lubricant films under and behind the drop can be a significant source of dissipation when drops move on lubricated surfaces[23,25]. Our heatmaps highlight that the dissipation associated with Landau-Levich film formation is predominantly localized in the transition region of the dynamic menisci (zones 2 and 5) rather than in the film deposited under the drop (zone 3) or behind the drop (beyond the left side of zone 5). A similar dissipation profile is observed in the classic Landau-Levich problem of pulling a plate out of a liquid bath, where dissipation occurs mostly in the transition region between the film and the dynamic meniscus[40]. Dissipation in the deposited film is relatively small compared to that in the transition region between the meniscus and the film since lubricant follows linear trajectories with relatively small velocity gradients in the film.

On average, across all the capillary numbers, the regions of the wetting ridge closest to the drop/lubricant interface (zones 2 and 4) contribute the most to the total dissipation (≈20–25%), followed by the regions containing the outer extremities of the wetting ridge (zones 3 and 5, ≈15% each). In total, the front wetting ridge (zones 1+2) and rear wetting ridge (zones 4+5)

contribute almost equally (within 5%) to the total dissipation. Thus, both sides of the wetting ridge are equally important to the friction force experienced by the drop.

Typically, the height of the rear wetting ridge is larger than that of the front wetting ridge. This asymmetry causes zones 4 + 5 to occupy a greater volume than zones 1 + 2. Furthermore, both the heights of the front and rear sides of the wetting ridge decrease with speed, causing all the zones, except zone 3, to become smaller at higher capillary numbers. Since the volumes of the different zones change with capillary number, we may expect the relative dominance of the dissipation per unit volume in the different regions to change with capillary number. However, it turns out that this is not the case. Indeed, when normalized per unit volume, the dissipation in the different zones barely changes with capillary number (Supplementary Fig. 10). However, since the volumes of the different zones differ, the relative ordering of the zones changes. On pillars, the normalized dissipation in zone 2 is the largest, followed by zones 1, 4, 5, and 3. The ordering of the different zones is similar on the flat surface, except that the normalized dissipation in zone 4 is larger than in zone 1.

Visualizing 3D dissipation onto a 2D plane. To represent the dissipation across the whole 3D domain visually onto a single image, we project the dissipation across all horizontal slices (80 in total) onto a single plane, as shown in Fig. 4a–d. This approach is advantageous compared to analyzing a single horizontal slice because it ensures that our conclusions are valid for the system as a whole rather than being specific to individual horizontal slices. The resultant heatmap shows clearly that dissipation in front and behind the drop is much stronger than at the sides on both surface geometries. In particular, over than 75% of the total dissipation lies within the pink dotted rectangle in Fig. 4c, d.

To further quantify how dissipation is distributed around the drop, we analyze the dissipation in a polar coordinate system (r, ϕ) with the origin located at the center-of-mass of the drop (Fig. 4c). When plotted against the azimuthal angle ϕ, the dissipation follows a double-well profile on both flat and pillar surfaces for all capillary numbers (Fig. 4e, f). These dissipation profiles have two maxima, a global maximum at the rear of the drop (at $\phi = -180^{\circ}$ and $\phi = 180^{\circ}$) and a local maximum at the front of the drop ($\phi = 0^{\circ}$). Furthermore, there are 2 minima, at the lateral sides of the drop ($\phi = -90^{\circ}$ and $\phi = 90^{\circ}$). Interestingly, the dissipation curves in Fig. 4e, f almost collapse onto a single master curve when normalized by the power supplied to move the drop (insets of Fig. 4e, f).

The fact that dissipation at the lateral sides is relatively small (below 25%) compared to dissipation along the axis of motion explains why simplified 2D simulations, which only consider dissipation along the axis of motion, reproduce the same scaling law between drop friction and capillary number as 3D simulations, as seen in Fig. 1a. Moreover, it also justifies why the dissipation mechanism proposed by Keiser et al.[23] has been so successful at explaining drop friction on LIS in 3D, despite only considering a single 2D cross-section of the drop and wetting ridge. However, the lateral flow around the drop in 3D changes the prefactor in Eq. (1) as well as the shape of the wetting ridge. Furthermore, in 2D, drop begins to oleoplane at lower capillary numbers than in 3D because there is no pathway for lubricant to flow around the drop. Thus, the 3D geometry is important to capture the details of the flow but is not necessary for modeling the friction force.

Shape of wetting ridge

In the simulations, the height of the wetting ridge decreases with capillary number. Furthermore, an asymmetry develops between the front and rear sides, with the front becoming smaller than the rear in 3D. This asymmetry has never been reported before, raising the question of whether it is a real effect. To answer this question, we image the dynamic wetting ridge using a bespoke setup based on laser scanning confocal microscopy[41]. Using a blade, we fix the position of the drop such that the wetting ridge remains within the field of view of the microscope at all times while the lubricated surface moves at constant velocities between 10 μm/s and 1 cm/s (Fig. 5a, Supplementary Movie 5). This procedure is equivalent to observing a drop moving along a stationary surface but is advantageous because it makes it possible to image motion over extended distances (several centimeters) despite the limited field of view of the microscope (<1 mm). It is crucial to image the wetting ridge over an extended distance to allow sufficient time for it to reach a steady state. Another advantage of this experimental setup is that it allows us to explore a much wider range of capillary numbers (4 orders of magnitude, 10^{-6} to 10^{-2}) than what is feasible with simulations.

To ensure that the blade does not interfere with the imaging, we always image the wetting ridge on the side opposite to the blade (as shown in Fig. 5a) and use large drops (volume 50 μL) to ensure the blade is at least ≈ 3 mm away from the field of view. All the experiments are performed using water drops and silicone oil lubricants with three different viscosities (10 cSt, 50 cSt, and 500 cSt). The solid surfaces consist of a rectangular array of cylindrical pillars (height 10 μm, diameter 30 μm, edge-to-edge spacing 30 μm, solid fraction 0.2). All the surfaces are infused with lubricant up to the top of the pillars (see Methods and Supplementary Methods for further details).

The experiments confirm the presence of an asymmetry between the front and rear wetting ridge, similar to what is seen in the simulations (Simulations: Fig. 5b, Experiments: Fig. 5c). Interestingly, there exists a critical speed, v_c, below which the shapes of the front and rear wetting ridges barely differ from their static shapes. This is reminiscent of the Landau-Levich problem of pulling a solid surface out of a liquid reservoir[42], where there exists a critical speed below which the shape of the meniscus between the liquid and the surface is independent of speed[40,43]. The meniscus in the Landau-Levich problem resembles the trailing side of the front and rear wetting ridges on LIS[25]. In the present problem here, the wetting ridge plays the role of the lubricant reservoir. At the front side of the wetting ridge, the drop/lubricant interface plays the role of the dynamic meniscus, whereas, at the rear side, the air/lubricant interface plays the role of the dynamic meniscus. In our experiments, the critical speed is smaller for the front side than the rear side of the wetting ridge. Above the critical speed, both the front and rear wetting ridges become smaller than their static size, but the asymmetry remains.

A typical experiment for the front wetting ridge, performed above the critical speed, is shown in Fig. 5d, e. As soon as the surface starts moving, the height of the wetting ridge quickly decreases and reaches a steady-state shape (region shaded green in Fig. 5e). Once the surface stops moving, the wetting ridge begins to gradually recover to its static shape. When conducting the experiments, we ensure that sufficient time is given between successive experiments to allow the wetting ridge to recover to its static shape.

In Fig. 5f, we systematically compare the evolution of the wetting ridge with speed by overlaying steady-state contours of the front wetting ridge at different speeds on a surface with 50 cSt lubricant. Each contour is obtained by averaging the shape of the wetting ridge over all the image frames that correspond to steady-state motion (at least 50 frames for each speed as shown by the green shaded region in Fig. 5e) (see Supplementary Note 1 and Supplementary Fig. 11 for details on image processing). This procedure averages out distortions in the shape of the wetting ridge due to noise and surface defects and eliminates the bias involved when having to choose a single frame as a representative image. Both the height and the width of the wetting ridge decrease by the same proportion as speed increases.

All the wetting ridge contours collapse onto a master contour when the horizontal and vertical axes are normalized by the height, h, of the dynamic wetting ridge (inset of Fig. 5f). Thus, the aspect ratio (height to width) is independent of velocity. When deriving scaling laws for the friction force, previous authors[8,23,24] have used a single velocity-independent length scale to characterize both the height and width of the wetting ridge. Our results demonstrate that although the assumption of a velocity-independent height and width is incorrect, the errors cancel out because the aspect ratio is constant.

We also extract the dynamic contact angle at the leading edge ('foot') of the front wetting ridge from the steady-state contours. The dynamic contact angle increases with capillary number according to a power law as hypothesized in

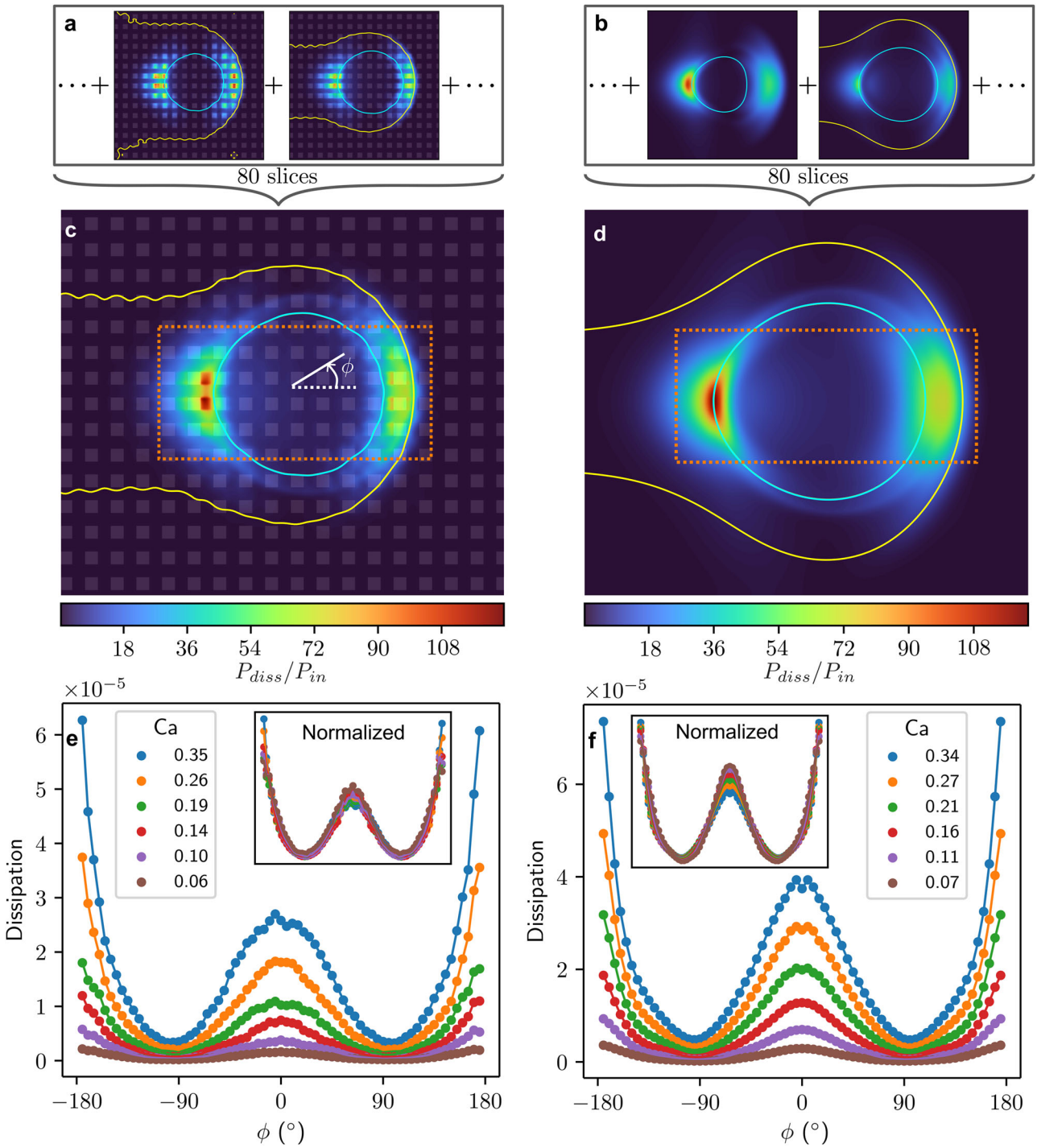

Fig. 4 | Projection of three-dimensional dissipation profiles onto a 2D image. The lubricant is 10 times more viscous than the drop. **a**, **b** Summing the dissipation in all horizontal slices for drops moving on lubricated surfaces with and without pillars to obtain the heatmaps in (**c**) and (**d**), respectively. The drop (cyan) and lubricant (yellow) contours in a single horizontal slice just above the initial lubricant height are shown as a guide to the eye to highlight the position of the drop and wetting ridge. The location of the pillars in (**a**) and (**b**) is shown as gray squares. In (a), Ca = 0.17 and in (b), Ca = 0.19. In both (**a**) and (**b**), the same body force is applied to the drop and the initial lubricant thickness is equal to the pillar height in (a). (**e**, **f**) Dissipation as a function of the azimuthal polar angle ϕ (defined in **c**) for different capillary numbers with (**e**) and without (**f**) pillars. For each ϕ, the dissipation is summed up over all polar radii, r. The dissipation has maxima in front ($\phi = 0^{\circ}$) and at the rear of the drop ($\phi = \pm 180^{\circ}$). ≈75% of the total dissipation in the lubricant lies within $\phi = \pm 40^{\circ}$ of the axis of motion (region highlighted by the dotted pink box in **c**). When the curves in (**e**) and (**f**) are normalized by the power input to move the drop, they collapse onto master curves, as shown in the insets.

previous studies[23,24]. However, our experiments suggest that the exponent of this power law is smaller than previously assumed. Depending on whether the contact angle is extracted by fitting a circle or a line to the lower part of the lubricant/air interface, we obtain an exponent between 0.08 and 0.21 compared to the previously assumed value of 0.33 (see Supplementary Note 2 and Supplementary Figs. 12–13 for details on the extraction of the dynamic contact angle). This suggests that the dynamics at the front of the wetting ridge may be more complex than previously hypothesized.

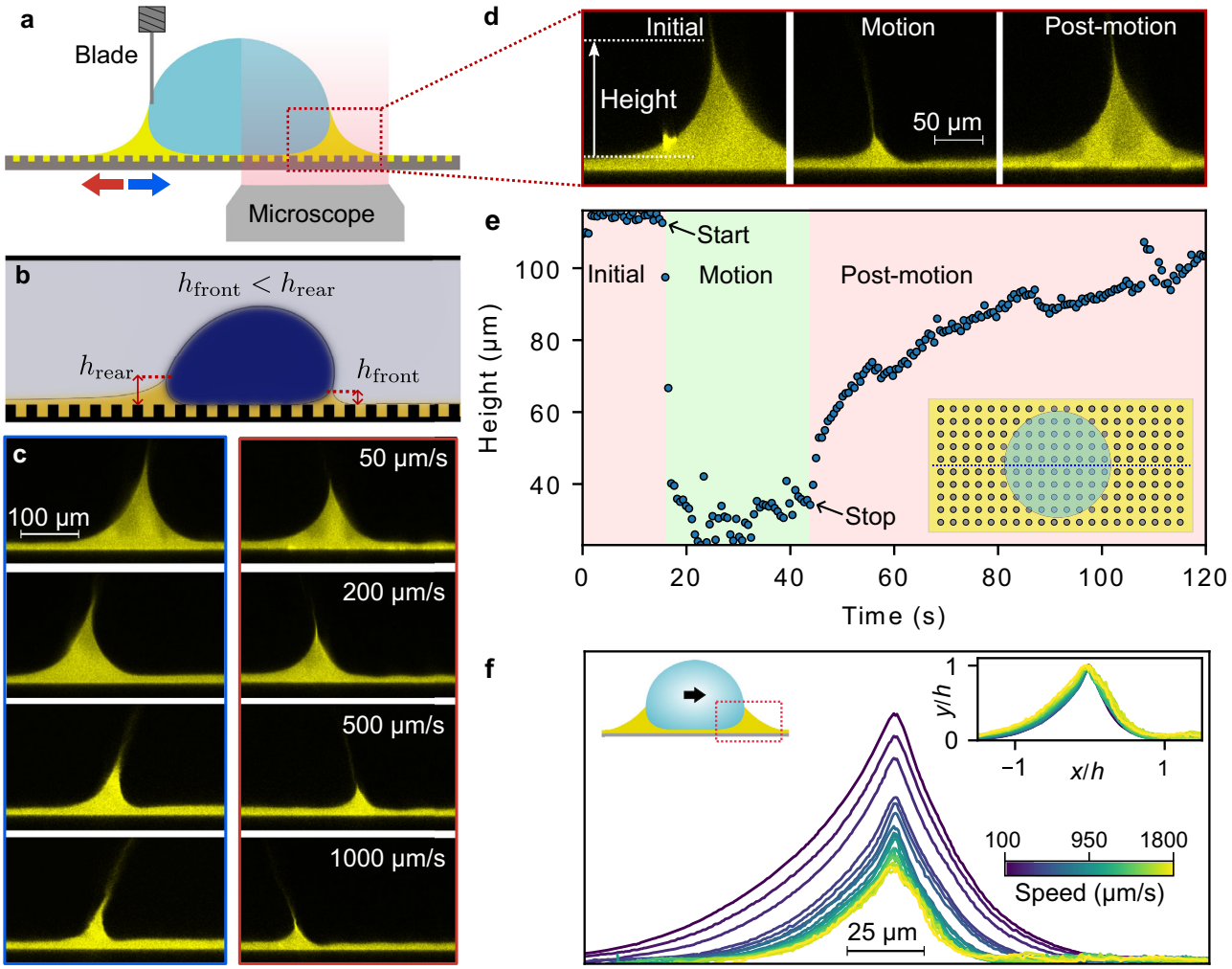

Fig. 5 | Shape of the dynamic wetting ridge. a Schematic of the experimental setup used to image the wetting ridge. By fixing the position of the drop above the objective lens of an inverted confocal microscope and moving the substrate at controlled speeds, we can continuously image the shape of the wetting ridge as a function of speed. An asymmetry between the front and rear wetting ridges is observed in both simulations (**b**) and experiments (**c**). In **c**, the left (right) column shows snapshots of the rear (front) wetting ridge at different speeds. **d** Image sequence of the front wetting ridge before, during, and after motion at 700 μm/s. Snapshots in (**c**, **d**) are taken in a vertical plane going between two rows of pillars across the center-of-mass of the drop, as shown in the top view schematic drawn in the inset of (**e**). The lubricant viscosity is 500 mPa s in (c) and (d). **e** Time evolution of wetting ridge height at 700 μm/s, with the corresponding snapshots are shown in (**d**). The surface starts moving at ≈15 s and stops at ≈ 43 s. **f** Contours of the front wetting ridge at a range of speeds (here the lubricant viscosity is 50 mPa s). The color of the contour denotes the shape of the wetting ridge at a given speed, as indicated by the color bar in the inset. Shorter and narrower contours correspond to higher speeds. Each contour is obtained by averaging the wetting ridge shape over all frames (>50) that correspond to steady-state motion (`Motion' region highlighted in green in **e**). The inset on the top right shows that all the contours collapse onto a master curve when the x and y axes are both normalized by the height of the dynamic wetting ridge.

For any given lubricant viscosity, the height and width of the wetting ridge follow similar trends with speed. However, the critical speed at which the wetting ridge begins to decrease in size decreases with increasing lubricant viscosity. In the following, we combine the effects of drop velocity and lubricant viscosity through the dimensionless lubricant capillary number, $Ca = \eta v/\gamma_{DL}$.

In general, the absolute height of the wetting ridge depends on several parameters, including the surface geometry, the lubricant thickness, and the surface tensions of the drop and lubricant[44–46]. For a given combination of liquids for the drop and lubricant on a surface with pillars, changes in the thickness of the lubricant layer relative to the height of the pillars has the largest influence on the size of the wetting ridge compared to changes in the height and width of the pillars [Supplementary Figs. 14–15]. For example, when the initial lubricant thickness is increased from 0.8 times the pillar height to 2 times the pillar height, the height of the wetting ridge increases by a factor of 2.5. The drop volume has a negligible influence on the height of the wetting ridge, as confirmed by experiments where we varied the drop volume by a factor of 60 (0.5 μL to 30 μL) and compared the height as a function of the drop volume [Supplementary Fig. 16].

Despite the variations in the absolute wetting ridge height with the lubricant thickness, a unified trend is obtained when the ratio between the dynamic height to the static height, h/h_0, is plotted against the normalized lubricant capillary number, Ca/Ca_c (Fig. 6). Here, h/h_0 is a measure of the amount by which the dynamic wetting ridge deviates from its static shape. Normalizing the dynamic height by h_0 allows us to unify results corresponding to different initial static wetting ridge heights, for example, due to different lubricant thicknesses. Ca is normalized by the critical capillary number, $Ca_c = \eta v_c/\gamma_{DL}$, which is the capillary number beyond which the height of the wetting ridge starts to decrease.

The results shown in Fig. 6 combine data from both experiments and simulations and include data over a wide range of lubricant viscosities, drop velocities, lubricant contact angles (fully wetting and partially wetting), surface geometries (flat and pillars), solid fractions, and lubricant thicknesses. Regardless of all these extensive parameter variations, h/h_0 follows a

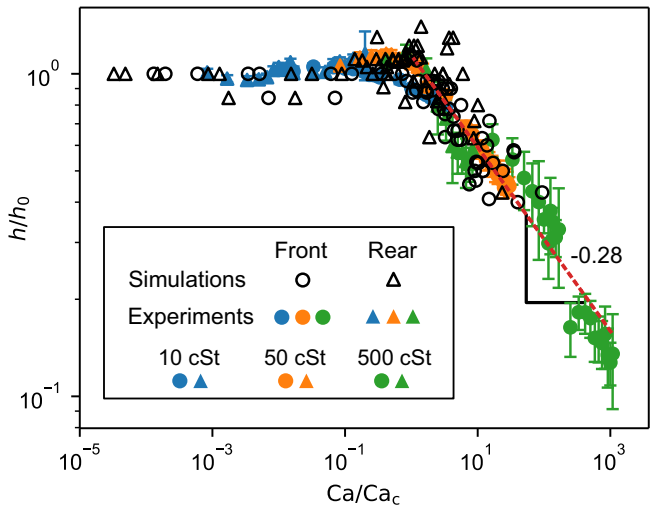

Fig. 6 | Scaling law for the height of the wetting ridge. A master curve is obtained for both the front and rear wetting ridges when the normalized height is plotted against the normalized capillary number (defined as the capillary number divided by the critical capillary number at which the height of the wetting ridge starts decreasing). The colored filled symbols correspond to experiments, and the black empty symbols correspond to simulations. Circles (triangles) correspond to the front (rear) wetting ridge. Each experimental data point corresponds to the average value of the normalized dynamic wetting ridge height across at least 50 image frames for each speed, and the error bar represents the standard deviation in the normalized height across these frames. The different colors of the experimental data points correspond to different lubricant viscosities, as shown in the figure legend. The simulations include data on different drop sizes ($R = 50$, 100 lattice units), different surface geometries (flat and pillars), different lubricant thicknesses (between 0.6 and 2 times the pillar height), different solid fractions of pillars (between 0.25 and 0.64), and both fully (0° contact angle) and partially wetting lubricants (contact angle 45° in air and under the drop).

remarkably universal scaling law above Ca_c,

$$h/h_0 \sim 1.1(\mathrm{Ca}/\mathrm{Ca_c})^{-0.28}. \quad (4)$$

We note that Ca_c is different for the front and rear wetting ridges and is smaller for the front wetting ridge.

The variation in size of the wetting ridge with speed has consequences on how much lubricant drops transport and deplete as they slide off LIS. Minimizing the depletion of lubricant by various external factors, such as sliding drops, shear flows, and lubricant evaporation, is the main challenge in the design of LIS since depletion leads to a degradation in the slippery property of LIS. When drops slide off LIS, they carry away lubricant via the wetting ridge. After the passage of a large number of drops, this can be a significant cause of depletion.

Based on our results, we can estimate how much lubricant is transported and depleted by the wetting ridge at different capillary numbers. Up to the the critical capillary number Ca_c ($\approx 10^{-4}$ in our experiments), the height, width, and thus volume, of the wetting ridge remain unchanged. Therefore, drops moving at capillary numbers below Ca_c transport the same amount of lubricant in their wetting ridge. However, above Ca_c, the volume of the wetting ridge decreases according to,

$$V \sim Rh^2 \sim Rh_0^2(\mathrm{Ca}/\mathrm{Ca_c})^{-0.56}. \quad (5)$$

Here, R is the base radius of the drop. We have used the fact that the width of the wetting ridge is proportional to its height and used Eq. (4) to express h as a function of Ca, omitting the prefactor.

According to Eq. (5), drops carry less lubricant in their wetting ridge when they move faster. For instance, a 4 times increase in drop speed leads to a reduction in the wetting ridge volume by a factor of ≈ 2. This provides an explanation for recent experimental data that highlighted a positive correlation between higher drop mobilities and a smaller amount of depletion[33]. Thus, technologies that utilize LIS should consider operating at high capillary numbers to minimize lubricant depletion via the wetting ridge. For drops driven by gravity, high capillary numbers can be achieved using large drops or positioning the surface at a large tilt angle with respect to the horizontal.

Conclusion

In summary, we have used lattice Boltzmann simulations to construct dissipation heatmaps to show where energy is dissipated locally when drops move on lubricated surfaces. Regardless of whether the solid substrate is flat or consists of an array of micropillars, the majority of energy is dissipated in the wetting ridge, directly in front and behind the drop. The pillars do not change the overall features in the dissipation heatmaps, demonstrating that the primary advantage of using lubricant-infused surfaces with micro/nanostructures is to increase capillary suction of the lubricant, and thus reduce lubricant depletion.

Dissipation at the lateral sides of the drop is only around 25%, suggesting that simplified 2D models that ignore the lateral sides effectively capture the most important dissipation regions. However, the full 3D drop geometry must be considered to accurately capture the flow of lubricant around the drop, the shape of the wetting ridge, and the thickness of the Laudau-Levich film underneath and behind the drop. By combining simulations and confocal microscopy experiments, we showed the size of the wetting ridge decreases with capillary number and an asymmetry develops between the front and rear sides. The reduction in the size of the wetting ridge at higher capillary numbers suggests that fast drops transport and deplete less lubricant than slow drops.

An interesting open question for future studies is to investigate the physical origins of the transition from a 2/3 to a 1/3 scaling law exponent between the friction force and the capillary number. Recently, Li et al.[35] used a simplified simulation setup (pulling a plate out of a confined liquid bath) to suggest that this scaling transition can be captured when the viscous stress in the meniscus is concentrated at the tail of the rear wetting ridge (corresponding to zone 5 in Fig. 3c). We expect this region to become more relevant when the lubricant film thickness is much smaller compared to the drop size, as is often the case in experiments but not in our current simulations.

Methods

Simulation method

We use a free energy lattice Boltzmann method to simulate the motion of drops on lubricant-infused surfaces[47,48]. The thermodynamics of the system is described by the following free energy functional,

$$F = \int_\Omega \Big[\frac{12}{\alpha}\left(\gamma_{12}C_1^2C_2^2 + \gamma_{13}C_1^2C_3^2 + \gamma_{23}C_2^2C_3^2 + C_1C_2C_3(S_1C_1 + S_2C_2 + S_3C_3)\right) + \frac{3}{8}\alpha S_1(\nabla C_1)^2 + \frac{3}{8}\alpha S_2(\nabla C_2)^2 + \frac{3}{8}\alpha S_3(\nabla C_3)^2 + \Lambda C_1^2C_2^2C_3^2\Big]\mathrm{d}V. \quad (6)$$

Here, $0 \le C_i \le 1$ ($i = 1, 2, 3$) are the relative concentrations of the fluid phases. We set $C_3 = 1 - C_1 - C_2$ in order to enforce the constraint that the relative concentrations must sum to 1. The form of the first term in brackets leads to 3 distinct bulk phases, corresponding to the 3 fluids (air, lubricant, drop). Interfacial tensions between the different fluids emerge from the next 3 terms (gradient terms). α controls the width of the diffuse interface between the different fluids. The final term makes it possible to capture positive spreading parameters, which allows us to simulate drops that are cloaked by a lubricant. $\Lambda \ge 0$ can be tuned to vary the energy penalty associated with the drop-lubricant-air contact line. The higher the value of Λ, the greater the energy associated with the drop-lubricant-air contact line, and therefore the more favorable it is for the lubricant to cloak the drop to eliminate the drop/

lubricant/air contact line when the spreading parameter of the lubricant on the drop is positive. The last term also improves numerical stability even when drops are not cloaked. The parameter S_i is related to the interfacial tensions γ_{ij} between 2 fluids according to,

$$S_i = \gamma_{ij} + \gamma_{ik} - \gamma_{jk}, \tag{7}$$

where i, j and $k = 1, 2, 3$ and $i \neq j \neq k$.

At the solid boundaries, the solid-fluid wetting interactions enter as a geometric boundary condition to account for the contact angles[49],

$$\mathbf{n} \cdot \nabla C_i = \sum\nolimits_{j=1}^{3} \xi_{ij} C_i C_j, \tag{8}$$

where $\mathbf{n}$ is a unit vector normal to the solid surface, and ξ_{ij} is related to the contact angles according to,

$$\xi_{ij} = \begin{cases} 0, & i = j \\ \frac{8}{\alpha}\left(\frac{\gamma_{i3}}{\gamma_{ij}}\cos\theta_{i3} - \frac{\gamma_{j3}}{\gamma_{ij}}\cos\theta_{j3}\right), & i, j = 1, 2; i \neq j. \end{cases} \tag{9}$$

Note that only 2 out of the 3 possible contact angles are independent. Therefore, setting θ_{13} and θ_{23} to the desired values, automatically sets θ_{12}, since these 3 angles are related by the Girifalco-Good relation[47],

$$\gamma_{12}\cos\theta_{12} + \gamma_{23}\cos\theta_{23} + \gamma_{13}\cos\theta_{13} = 0. \tag{10}$$

To solve for the dynamics of the ternary fluid system described by Eq. (6), we used a lattice Boltzmann algorithm based on the method described in a previous study[48] using a D3Q19 velocity set. This model uses higher-order gradient calculations to reduce nonphysical velocities at the fluid interface, which is characteristic of diffuse interface models. The aforementioned approach improves the accuracy of the velocities used in the viscous dissipation calculation. The no-slip condition on the solid wall is enforced through the halfway bounce-back scheme, which enforces a Dirichlet condition of zero velocity on the boundary[50].

In the lattice Boltzmann framework, the components of the viscous stress tensor can be obtained directly from the lattice Boltzmann distribution functions according to[50]

$$\sigma_{\alpha\beta} \approx -\left(1 - \frac{\Delta t}{2\tau}\right)\left[\sum\nolimits_i c_{i\alpha} c_{i\beta}\left(f_i - f_i^{\mathrm{eq}}\right) + \frac{\Delta t}{2}\left(F_\alpha v_\beta + F_\beta v_\alpha\right)\right]. \tag{11}$$

Here, α and β correspond to the x, y, or z directions, Δt is the discrete time step, τ is the relaxation time which is related to the fluid viscosity, $c_{i\alpha}$ are components of the discrete D3Q19 velocity set, f_i (i = 1-19) are the distribution functions, f_i^{eq} are the equilibrium distribution functions, and F_α is the external body force driving the motion of the drop along the surface. The components of the viscous stress tensor for a typical simulation are shown in Supplementary Fig. 3.

Simulation setup

We initialized the drop as a hemisphere with a radius of 50 lattice units on top of the lubricant film. The initial lubricant thickness was 5 lattice units (equal to the height of pillars). On surfaces with pillars, the dimensions of the pillars were 5 × 5 × 5 lattice units, with an edge-to-edge spacing of 5 lattice units. The 3D simulation domain was up to 750 × 150 × 75 lattice units and the 2D simulation domain was up to 750 × 150 lattice units. We applied a horizontal body force (between 5×10^{-7} and 3.5×10^{-6} per unit volume) to the drop and waited for its center-of-mass velocity to reach a steady state before analyzing the energy dissipation heatmaps. We ran the 3D simulations for 350,000 time steps, which took ≈72 h on 128 CPU cores (AMD EPYC 7702) per simulation on the Durham University Hamilton HPC. The 2D simulations were run for up to 1 million time steps.

We used the following simulation parameters (all in lattice units). Here, we denote 1 as the drop phase, 2 as the air phase, and 3 as the lubricant phase. For the interfacial tensions, we use $\gamma_{12} = 0.0104$, $\gamma_{13} = 0.006685$, and $\gamma_{23} = 0.003785$. These interfacial tensions were chosen such that we obtain a Neumann angle of 10° at the tip of the wetting ridge, which is equal to the experimentally measured apparent angle of ≈10° (Supplementary Fig. 12). In most of the simulations, the relaxation times of the lattice Boltzmann distribution functions are $\tau_1 = 0.778$, $\tau_2 = 0.505$, $\tau_3 = 3.278$. To test the effect of varying the lubricant/drop viscosity ratio, some simulations were also performed with a reduced value of $\tau_1 = 0.51$ while keeping τ_2 and τ_3 the same as before. The relaxation times are related to the dynamic viscosities of the fluids according to

$$\eta_i = \rho c_s^2\left(\tau_i - \frac{\Delta t}{2}\right), \tag{12}$$

where ρ is the fluid density ($\rho = 1$ in our equal density model), $c_s = 1/\sqrt{3}$ is the speed of sound in lattice Boltzmann framework, $\Delta t = 1$ is the discretized time step, and i = 1, 2 or 3 corresponds to the 3 different fluids. Note that using an equal density model is justified for this study because density differences are not important when viscous effects dominate inertial effects. For simulations where the lubricant/drop viscosity ratio was 10, we used $\eta_1 = 0.09266$, $\eta_2 = 0.00167$, and $\eta_3 = 0.9266$. To increase the lubricant/drop viscosity ratio to 278 in some of the simulations, we reduced η_1 to 0.00333 while keeping the other viscosities unchanged. At the solid walls, the two independent contact angles are $\theta_{13} = 180°$ and $\theta_{23} = 180°$ (fully wetting lubricant).

Due to the diffuse fluid interfaces inherent in our model, we expect the total drop dissipation calculated in Fig. 1b to be a slight overestimate (few %) of the true value. Close to the drop/lubricant diffuse interface, dissipation in the lubricant phase may leak across the interface and into the drop phase. However, this does not change our conclusion that dissipation in the lubricant dominants because, even with the diffuse interface, the amount of energy dissipated in the lubricant remains over 2 times higher than in the drop across the whole range of capillary numbers.

Experimental procedures

We synthesized cylindrical SU-8 micropillars on microscope coverslips using photolithography. The micropillars had a height of 10 μm, diameter of 30 μm, and the edge-to-edge spacing between two adjacent pillars was 30 μm. The micropillars were then sprayed with hydrophobic nanoparticles (Glaco99) before being infused up to the pillar height with silicone oil containing an in-house fluorescent dye using the capillary wicking method (see Supplementary Methods for more details). The fluorescent dye was a hydrophobic perylene monoimide dye (PMI) at a concentration of around 0.05 mg/mL. The dye is compatible with silicone oil and does not change the surface tension of the oil[6,18,51].

We then placed Milli-Q water drops on the surface and imaged the wetting ridge using a laser scanning confocal microscope (Leica TCS SP8) with a spatial resolution between 0.7 μm and 2.5 μm along both the horizontal and vertical directions and a temporal resolution between 1 and 3 frames per second. The spatial resolution was chosen to maximize the image quality while not compromising on the required temporal resolution.

Silicone oil has a positive spreading parameter ($S = \gamma_{\mathrm{DA}} - \gamma_{\mathrm{DL}} - \gamma_{\mathrm{LA}}$, where γ_{DA}, γ_{DL}, and γ_{LA} are the interfacial tension of the drop/air, drop/lubricant, and lubricant/air interfaces, respectively) on water and thus forms a cloak around the drop. While it is possible to image the cloak under static conditions by performing careful experiments (e.g., see Supplementary Fig. 17), it is difficult to do so during dynamic measurements. Thus, our experimental analysis of the wetting ridge focuses only on the wetting ridge and neglects the cloak.

Data availability

The datasets generated during and/or analyzed during the current study are available from the corresponding authors upon reasonable request.

Code availability

The ternary lattice Boltzmann code used in the current study is available from the corresponding authors on reasonable request.

Received: 15 May 2024; Accepted: 5 September 2024;
Published online: 17 September 2024

References

1. Dowson, D. *History of Tribology* (Longman, 1979).
2. Butt, H.-J. & Kappl, M. *Surface and Interfacial Forces* (Wiley-VCH, 2018), second edn.
3. Quéré, D. Non-sticking drops. *Rep. Prog. Phys.* **68**, 2495–2532 (2005).
4. Wong, T.-S. et al. Bioinspired self-repairing slippery surfaces with pressure-stable omniphobicity. *Nature* **477**, 443–447 (2011).
5. Lafuma, A. & Quéré, D. Slippery pre-suffused surfaces. *EPL* **96**, 56001 (2011).
6. Schellenberger, F. et al. Direct observation of drops on slippery lubricant-infused surfaces. *Soft Matter* **11**, 7617–7626 (2015).
7. Bottone, D. & Seeger, S. Droplet memory on liquid-infused surfaces. *Langmuir* **39**, 6160–6168 (2023).
8. David Smith, J. et al. Droplet mobility on lubricant-impregnated surfaces. *Soft Matter* **9**, 1772–1780 (2013).
9. Li, J., Ueda, E., Paulssen, D. & Levkin, P. A. Slippery lubricant-infused surfaces: properties and emerging applications. *Adv. Funct. Mater.* **29**, 1802317 (2019).
10. Villegas, M., Zhang, Y., Abu Jarad, N., Soleymani, L. & Didar, T. F. Liquid-infused surfaces: a review of theory, design, and applications. *ACS Nano* **13**, 8517–8536 (2019).
11. Park, K.-C. et al. Condensation on slippery asymmetric bumps. *Nature* **531**, 78–82 (2016).
12. Sundin, J., Ciri, U., Leonardi, S., Hultmark, M. & Bagheri, S. Heat transfer increase by convection in liquid-infused surfaces for laminar and turbulent flows. *J. Fluid Mech.* **941**, A9 (2022).
13. Howell, C., Grinthal, A., Sunny, S., Aizenberg, M. & Aizenberg, J. Designing liquid-infused surfaces for medical applications: a review. *Adv. Mater.* **30**, 1802724 (2018).
14. Badv, M., Imani, S. M., Weitz, J. I. & Didar, T. F. Lubricant-infused surfaces with built-in functional biomolecules exhibit simultaneous repellency and tunable cell adhesion. *ACS Nano* **12**, 10890–10902 (2018).
15. Geyer, F. et al. When and how self-cleaning of superhydrophobic surfaces works. *Sci. Adv.* **6**, eaaw9727 (2020).
16. Heckenthaler, T. et al. Self-cleaning mechanism: why nanotexture and hydrophobicity matter. *Langmuir* **35**, 15526–15534 (2019).
17. Yu, C. et al. Nature–Inspired self–cleaning surfaces: mechanisms, modelling, and manufacturing. *Chem. Eng. Res. Des.* **155**, 48–65 (2020).
18. Papadopoulos, P., Mammen, L., Deng, X., Vollmer, D. & Butt, H.-J. How superhydrophobicity breaks down. *Proc. Natl. Acad. Sci. USA* **110**, 3254–3258 (2013).
19. Mouterde, T., Raux, P. S., Clanet, C. & Quéré, D. Superhydrophobic frictions. *Proc. Natl. Acad. Sci. USA* **116**, 8220–8223 (2019).
20. Wang, D. et al. Design of robust superhydrophobic surfaces. *Nature* **582**, 55–59 (2020).
21. Lafuma, A. & Quéré, D. Superhydrophobic states. *Nat. Mater.* **2**, 457–460 (2003).
22. Liimatainen, V. et al. Mapping microscale wetting variations on biological and synthetic water-repellent surfaces. *Nat. Commun.* **8**, 1798 (2017).
23. Keiser, A., Baumli, P., Vollmer, D. & Quéré, D. Universality of friction laws on liquid-infused materials. *Phys. Rev. Fluids* **5**, 014005 (2020).
24. Keiser, A., Keiser, L., Clanet, C. & Quéré, D. Drop friction on liquid-infused materials. *Soft Matter* **13**, 6981–6987 (2017).
25. Daniel, D., Timonen, J. V. I., Li, R., Velling, S. J. & Aizenberg, J. Oleoplaning droplets on lubricated surfaces. *Nat. Phys.* **13**, 1020–1025 (2017).
26. Kreder, M. J. et al. Film dynamics and lubricant depletion by droplets moving on lubricated surfaces. *Phys. Rev. X* **8**, 031053 (2018).
27. Nath, S. & Quéré, D. Spreading of water on a liquid-infused solid. *Phys. Rev. Fluids* **7**, 084003 (2022).
28. Hardt, S. & McHale, G. Flow and drop transport along liquid-infused surfaces. *Annu. Rev. Fluid Mech.* **54**, 83–104 (2022).
29. Sadullah, M. S., Semprebon, C. & Kusumaatmaja, H. Drop dynamics on liquid-infused surfaces: the role of the lubricant ridge. *Langmuir* **34**, 8112–8118 (2018).
30. Sadullah, M. S., Panter, J. R. & Kusumaatmaja, H. Factors controlling the pinning force of liquid droplets on liquid infused surfaces. *Soft Matter* **16**, 8114–8121 (2020).
31. Baumli, P. et al. The challenge of lubricant-replenishment on lubricant-impregnated surfaces. *Adv. Colloid Interface Sci.* **287**, 102329 (2021).
32. Wexler, J. S., Jacobi, I. & Stone, H. A. Shear-driven failure of liquid-infused surfaces. *Phys. Rev. Lett.* **114**, 168301 (2015).
33. Laney, S. K. et al. Delayed lubricant depletion of slippery liquid infused porous surfaces using precision nanostructures. *Langmuir* **37**, 10071–10078 (2021).
34. Peppou-Chapman, S., Hong, J. K., Waterhouse, A. & Neto, C. Life and death of liquid-infused surfaces: a review on the choice, analysis and fate of the infused liquid layer. *Chem. Soc. Rev.* **49**, 3688–3715 (2020).
35. Li, K., Lv, C. & Feng, X.-Q. Rapid droplet leads the liquid-infused slippery surfaces more slippery (2023). arXiv:2309.02038.
36. Li, X. et al. Kinetic drop friction. *Nat. Commun.* **14**, 4571 (2023).
37. Stetten, A. Z., Golovko, D. S., Weber, S. A. L. & Butt, H.-J. Slide electrification: charging of surfaces by moving water drops. *Soft Matter* **15**, 8667–8679 (2019).
38. Butt, H.-J., Berger, R., Steffen, W., Vollmer, D. & Weber, S. A. L. Adaptive wetting-adaptation in wetting. *Langmuir* **34**, 11292–11304 (2018).
39. Succi, S. *The Lattice Boltzmann Equation: For Complex States of Flowing Matter* (Oxford University Press, Oxford, UK, 2018), 1 ed.
40. Cantat, I. Liquid meniscus friction on a wet plate: Bubbles, lamellae, and foamsa). *Phys. Fluids* **25**, 031303.
41. Naga, A. et al. How a water drop removes a particle from a hydrophobic surface. *Soft Matter* **17**, 1746–1755 (2021).
42. Rio, E. & Boulogne, F. Withdrawing a solid from a bath: how much liquid is coated? *Adv. Colloid Interface Sci.* **247**, 100–114 (2017).
43. Teletzke, G. F., Davis, H. T. & Scriven, L. E. Wetting hydrodynamics. *Rev. Phys. Appl. (Paris)* **23**, 989–1007 (1988).
44. Semprebon, C., McHale, G. & Kusumaatmaja, H. Apparent contact angle and contact angle hysteresis on liquid infused surfaces. *Soft Matter* **13**, 101–110 (2016).
45. Dai, Z. & Vella, D. Droplets on lubricated surfaces: the slow dynamics of skirt formation. *Phys. Rev. Fluids* **7**, 054003 (2022).
46. Semprebon, C., Sadullah, M. S., McHale, G. & Kusumaatmaja, H. Apparent contact angle of drops on liquid infused surfaces: geometric interpretation. *Soft Matter* **17**, 9553–9559 (2021).
47. Semprebon, C., Krüger, T. & Kusumaatmaja, H. Ternary free-energy lattice Boltzmann model with tunable surface tensions and contact angles. *Phys. Rev. E* **93**, 033305 (2016).
48. Haghani Hassan Abadi, R., Fakhari, A. & Rahimian, M. H. Numerical simulation of three-component multiphase flows at high density and viscosity ratios using lattice Boltzmann methods. *Phys. Rev. E* **97**, 033312 (2018).
49. Dong, S. Wall-bounded multiphase flows of N immiscible incompressible fluids: consistency and contact-angle boundary condition. *J. Comput. Phys.* **338**, 21–67 (2017).
50. Krüger, T. et al. *The Lattice Boltzmann Method: Principles and Practice*. Graduate Texts in Physics (Springer International Publishing, Cham, Switzerland, 2016), 1 edn. https://doi.org/10.1007/978-3-319-44649-3

51. Cai, Z., Skabeev, A., Morozova, S. & Pham, J. T. Fluid separation and network deformation in wetting of soft and swollen surfaces. *Commun. Mater.* **2**, 1–11 (2021).

Acknowledgements

We thank Anke Kaltbeitzel for technical support with the experiments, and Ciro Semprebon and Rodrigo Ledesma Aguilar for stimulating discussions. We acknowledge funding from the EPSRC National Fellowships in Fluid Dynamics Grant No. EP/X028410/1 (A.N.), an EPSRC Grant No. EP/V034154/1 (A.N., M.R., H.K.), the EU HORIZON research and innovation program under the Marie Skłodowska-Curie grant agreement No. 101062409 (W.S.Y.W.), the Academy of Finland grant agreement No. 13347247 (W.S.Y.W.).

Author contributions

A.N., D.V., and H.K. conceptualized the project; A.N. and M.R. designed and performed the simulations and analyzed the simulation data, supported by H.K; A.N., and D.V. conceptualized the experimental setup for visualizing the dynamic wetting ridge; A.N. performed the experiments and analyzed the experimental data, supported by W.S.Y.W., L.H., and D.V.; A.S-A. and W.S.Y.W. fabricated the micropillars for the experiments; A.N. designed the figures and wrote the paper with contributions from all authors. All authors contributed to interpreting the results of the study and editing the paper.

Competing interests

The authors declare no competing interests.

Additional information

Supplementary information The online version contains supplementary material available at https://doi.org/10.1038/s42005-024-01795-3.

Correspondence and requests for materials should be addressed to Abhinav Naga, Doris Vollmer or Halim Kusumaatmaja.

Peer review information *Communications Physics* thanks Youhua Jiang and the other anonymous reviewer(s) for their contribution to the peer review of this work. A peer review file is available.